Coupling of Aerodynamic and Dynamic Methods for the Calculation of Helicopter Rotors in Forward Flight

B. Buchtala, D. Wehr, and S. Wagner
Institut für Aerodynamik und Gasdynamik, Universität Stuttgart
Pfaffenwaldring 21, 70550 Stuttgart, Germany

Abstract

An approach for the numerical simulation of the aeroelastic behaviour of a helicopter rotor in forward flight is presented. For this purpose a structural dynamic model of the blade, STAN, is coupled with a three–dimensional finite volume Euler solver for unsteady compressible flows, INROT.

The solution of the coupled system is found by the use of staggered time–marching procedures. Two fundamentally different coupling schemes are investigated.

The validation of the developed method is done on a BO–105 model rotor investigated at the DNW within the framework of the HELINOISE research project.

Nomenclature

A, **B**, **C**	jacobian matrices of fluxes
c_d	damping parameter
c_f	spring stiffness
D	diagonal matrix
$\tilde{\bar{e}}$	specific total absolute energy
e, **f**, **g**	flux vectors in ξ, η, ζ direction
$\mathbf{f}_\mathrm{l}$	aerodynamic force vector
$\mathcal{F}$	right–hand side of blade dynamics
i	index of blade degrees of freedom
i, j, k	grid index in ξ, η, ζ direction
I	identity matrix
k	Coriolis and centrifugal force vector
L	lower triangular matrix
LHS	left–hand side matrix
m	mass
$\mathbf{m}_\mathrm{l}$	aerodynamic moment vector
$\mathbf{m}_\mathrm{m}$	mass moment of inertia vector
$\mathbf{m}_\mathrm{f}$	spring moment vector
$\mathbf{m}_\mathrm{d}$	damper moment vector
n	number of degrees of freedom index of time step
p	pressure
Q	jacobian matrix of k
r	coordinate vector
rhs	right–hand side vector
S	blade surface
t	time
$\bar{u}, \bar{v}, \bar{w}$	absolute velocities
U	upper triangular matrix
v	velocity vector
V	blade volume, cell volume
w_i	induced velocity
β	flapping angle
δ	degrees of freedom vector
ε	upper error bound
ζ	lagging angle
σ	spectral radius
τ	time
ξ, η, ζ	body–fitted coordinates
ϕ	conservative variables vector
ψ	azimuth angle
ω	angular velocity vector

Introduction

A key component for the realistic simulation of helicopter flight is the accurate calculation of the aerodynamic and dynamic behaviour of the rotor blades. Today's aerodynamic methods are ranging from blade–element theory with prescribed or fixed wake geometry over potential methods to Euler and Navier–Stokes solvers. On the other hand, the dynamic behaviour of the rotor blades can be calculated by multiple rigid–body systems up to flexible body systems by means of finite–element methods. For the accurate prediction of the rotor flow field, rotor loads, trim conditions, stability characteristics and the simulation of flight manoeuvres the coupling of such aerodynamic and dynamic methods is necessary.

Solution Procedures

Elastic Modelling of the Rotor Blade

The dynamic behaviour of the blades is represented by their first natural modes and frequencies. Since the calculation model takes into account rotor systems with articulated and flexible blades, the rotor is modelled as a dynamic system of multiple rigid bodies connected with hinges. The hinges are provided with springs and dampers. Their characteristics represent the elastic properties of the blade. Figure 1 shows an art impression of the possible degrees of freedom of a single rotor blade: control torsion angle ϑ_e, flapping angle β, lagging angle ζ, and blade torsion angle ϑ_b.

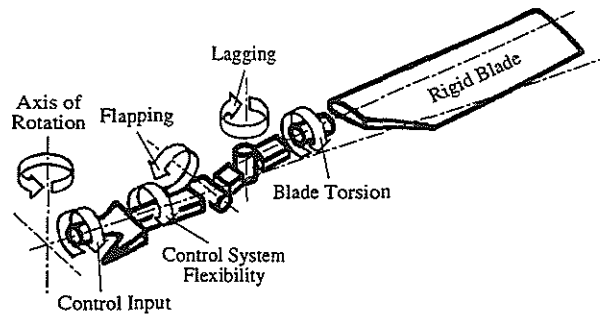

Figure 1: Model of the Rotor Blade [4]

Although the dynamic model is not capable of predicting nonlinear aeroelastic effects such as flutter, it has been demonstrated in [8] that the consideration of only the first bending mode shapes is sufficient for the investigation of typical flight characteristics.

Let us now take a closer look at the derivation of the governing equations of blade motion. The equations are deduced from the momentum balances at the hinges. The outer moments (aerodynamic moments $\mathbf{m}_l$ and mass moments of inertia $\mathbf{m}_m$) are in equilibrium with the inner moments (spring moments $\mathbf{m}_f$ and damper moments $\mathbf{m}_d$), which leads to

$$\mathbf{m}_{l_i} + \mathbf{m}_{m_i} + \mathbf{m}_{f_i} + \mathbf{m}_{d_i} = 0 \qquad (1)$$

for an individual hinge i, each one representing a degree of freedom.

The **aerodynamic force and moment** of the rotor blade can be obtained in several ways with an increasing degree of complexity. The easiest way to determine the aerodynamic forces and moments is by means of the blade–element theory. This approach is described in detail by Buchtala in [1]. The aim of the present approach is to provide these forces and moments by solving the complete inviscid flow field around the rotor blade. How this is done will be outlined later in the section 'Aerodynamic Analysis'.

If we consider, for the moment, the inviscid flow field to be known, the demanded aerodynamic force and moment with respect to the quarter chord point at the blade root, QC, is given by

$$\mathbf{f}_{l_{QC}} = \iint_S p \, d\mathbf{n} \qquad (2)$$

$$\mathbf{m}_{l_{QC}} = \iint_S \mathbf{r}_{QCP} \times p \, d\mathbf{n} \, . \qquad (3)$$

The integration is carried out over the entire blade surface S with the pressure p acting on the surface at point P. $\mathbf{r}_{QCP}$ is the coordinate vector pointing from QC to P.

REMARK 1 No matter how the aerodynamic forces and moments are determined, each of these methods needs as a basic requirement the velocity of arbitrary points on the blade. The velocity–winder of the quarter chord point at the blade root, relative to the rotating rotor hub system, can be expressed as

$$\mathbf{v}_{QC} = \sum_{i=1}^{n} \boldsymbol{\omega}_i \times \mathbf{r}_{iQC} \qquad (4)$$

$$\boldsymbol{\omega}_{QC} = \sum_{i=1}^{n} \boldsymbol{\omega}_i \, . \qquad (5)$$

Here $\mathbf{r}_{iQC}$ is the position vector from the hinge i to the quarter chord point, $\boldsymbol{\omega}_i$ is the vector of the angular velocity – the derivative of the degree of freedom – at hinge i. The summation is carried out over n degrees of freedom. In fact, the position of the rigid blade and the velocity–winder defined by Equations (4) and (5) constitute the first part of the interface in the fluid

structure coupling process. With the velocity–winder known, the velocity of any point P, holding a fixed position relative to QC, can be calculated using

$$\mathbf{v}_P = \mathbf{v}_{QC} + \boldsymbol{\omega}_{QC} \times \mathbf{r}_{QCP} \,. \tag{6}$$

The **mass moment of inertia** is defined as

$$\mathbf{m}_{\mathbf{m}_{QC}} = -\iiint_V \mathbf{r}_{QCP} \times \mathbf{b}\, dm \,. \tag{7}$$

The derivation of the acceleration vector $\mathbf{b}$ and the subsequent integration (7) involves quite tedious computations. The details can therefore be found in [1].

The dynamic model of the blade uses springs and dampers to simulate the elastic properties of the blade. The resulting **inner moments** at the hinges are expressed as

$$\mathbf{m}_{\mathbf{f}_i} = -c_{\mathbf{f}_i} \cdot \delta_i \tag{8}$$

$$\mathbf{m}_{\mathbf{d}_i} = -c_{\mathbf{d}_i} \cdot \dot{\delta}_i \tag{9}$$

with δ_i representing the ith degree of freedom.

Introducing Equations (3), (7), (8), and (9) in (1) the resulting second–order system of ordinary differential equations reads

$$\ddot{\boldsymbol{\delta}} = \mathcal{F}(\boldsymbol{\delta}, \dot{\boldsymbol{\delta}}, \mathbf{f}_{\mathbf{l}_{QC}}, \mathbf{m}_{\mathbf{l}_{QC}}) \,. \tag{10}$$

After transforming this system of second–order differential equations into an equivalent system of first–order differential equations, it can be solved by standard integration schemes. Here we used the explicit fourth–order Runge–Kutta method.

REMARK 2 It should be emphasized that the aerodynamic forces and moments themselves depend on $\boldsymbol{\delta}$ and $\dot{\boldsymbol{\delta}}$ (see Remark 1). However, they are explicitly shown since they represent the second interface between the dynamic and the aerodynamic solution procedures.

During the process of numerically integrating Equation (10) over a rotor revolution, the right–hand side $\mathcal{F}$ has to be evaluated several times. This is the most time–consuming part of the solution process, since this evaluation implies solving the governing equations for inviscid flow fields, i.e. the Euler equations. It is therefore of great importance to keep the number of evaluations of $\mathcal{F}$ as small as possible. A straightforward implementation of the fourth order Runge–Kutta method requires four evaluations of $\mathcal{F}$, and therefore of $\mathbf{f}_{\mathbf{l}_{QC}}$ and $\mathbf{m}_{\mathbf{l}_{QC}}$, for a single time step. Since this would be computationally unreasonable, the following approach was adopted: The first evaluation of the right–hand side per time step is done exactly. All other evaluations of $\mathcal{F}$ use an extrapolation of the aerodynamic forces and moments from the previous time steps, whereas the relatively cheap computations of the other terms on the right–hand side due to the mass moments of inertia are still done exactly. The benefit of this approach is that the results, using a time step sufficiently small for the aerodynamic analysis, differ with less than 0.01% in magnitude and that the computational time is reduced to a fourth.

Aerodynamic Analysis

The Euler solver has been extensively described in [10] and is shortly summarized here.

The Euler equations are formulated in body–fitted coordinates in a rotating frame of reference, which is attached to the z–axis, representing the rotor shaft:

$$\frac{\partial \boldsymbol{\phi}}{\partial \tau} + \frac{\partial \mathbf{e}}{\partial \xi} + \frac{\partial \mathbf{f}}{\partial \eta} + \frac{\partial \mathbf{g}}{\partial \zeta} = \mathbf{k} \,. \tag{11}$$

The vector of the conservative variables, multiplied by the cell volume, is given by

$$\boldsymbol{\phi} = V \cdot (\rho, \rho\bar{u}, \rho\bar{v}, \rho\bar{w}, \bar{\bar{e}}) \,. \tag{12}$$

The velocity and energy are given in terms of absolute velocities.

The time integration is performed by a second–order three point backward–difference scheme. This leads to the following implicit system of

equations

$$\frac{3}{2}\frac{\phi^{n+1}-\phi^n}{\Delta\tau}-\frac{1}{2}\frac{\phi^n-\phi^{n-1}}{\Delta\tau}+$$
$$\mathrm{e}_\xi^{n+1}+\mathrm{f}_\eta^{n+1}+\mathrm{g}_\zeta^{n+1}-\mathrm{k}^{n+1}\quad=0 \qquad (13)$$

which is iteratively solved by the Newton–Method. This leads to

$$\underbrace{\left[\frac{\mathbf{I}}{\Delta\tau}+\frac{2}{3}\left(\mathbf{A}_\xi^\mu+\mathbf{B}_\eta^\mu+\mathbf{C}_\zeta^\mu-\mathbf{Q}^\mu\right)\right]}_{\mathbf{LHS}}\Delta\phi^{\mu+1}=$$
$$\underbrace{-\left[\frac{\phi^\mu-\phi^n}{\Delta\tau}-\frac{1}{3}\frac{\phi^n-\phi^{n-1}}{\Delta\tau}\right.}_{\mathbf{rhs}}$$
$$\left.+\frac{2}{3}\left(\mathrm{e}_\xi^\mu+\mathrm{f}_\eta^\mu+\mathrm{g}_\zeta^\mu-\mathrm{k}^\mu\right)\right] \qquad (14)$$

where μ denotes the index of the subiteration within the time step. $\mathbf{A}$, $\mathbf{B}$, $\mathbf{C}$, and $\mathbf{Q}$ are the jacobian matrices of the fluxes, and the source term, respectively.

The LUSGS (Lower–Upper–Symmetric–Gauss–Seidel) implicit operator by Jameson and Yoon [5], applied by Chen, McCroskey and Obayashi [2] to rotating flows, is used for the solution of the resulting system of equations. It consists of an approximate factorization in lower $\mathbf{L}$, diagonal $\mathbf{D}$, and upper matrices $\mathbf{U}$. Defining $\Delta_{\xi,\eta,\zeta}$ and $\nabla_{\xi,\eta,\zeta}$ as forward– and backward–differences in the three coordinate directions, the matrices are written as

$$\mathbf{L}=\mathbf{I}+\gamma\Delta\tau\left(-\mathbf{A}_{ijk}^-+\nabla_\xi\mathbf{A}^+-\mathbf{B}_{ijk}^-+\nabla_\eta\mathbf{B}^+\right.$$
$$\left.-\mathbf{C}_{ijk}^-+\nabla_\zeta\mathbf{C}^+\right) \qquad (15)$$

$$\mathbf{D}=\left[\mathbf{I}+\gamma\Delta\tau\left(\mathbf{A}_{ijk}^+-\mathbf{A}_{ijk}^-+\mathbf{B}_{ijk}^+-\mathbf{B}_{ijk}^-\right.\right.$$
$$\left.\left.+\mathbf{C}_{ijk}^+-\mathbf{C}_{ijk}^-\right)\right]^{-1} \qquad (16)$$

$$\mathbf{U}=\mathbf{I}+\gamma\Delta\tau\left(\mathbf{A}_{ijk}^++\Delta_\xi\mathbf{A}^-+\mathbf{B}_{ijk}^++\Delta_\eta\mathbf{B}^-\right.$$
$$\left.+\mathbf{C}_{ijk}^++\Delta_\zeta\mathbf{C}^-\right) \qquad (17)$$

For the chosen time discretization γ is set to $2/3$. A simplified calculation of the split matrices can be carried out using

$$\mathbf{A}^\pm=\frac{1}{2}\left(\mathbf{A}\pm\sigma_\xi\mathbf{I}\right), \qquad (18)$$

where σ_ξ is the spectral radius of $\mathbf{A}$ multiplied by a factor $k\geq 1$.

Since the three matrices consist only of scalar diagonal 5×5 submatrices, which means that only divisions are necessary for the solution, the following equation

$$\mathbf{L}\cdot\mathbf{D}\cdot\mathbf{U}\,\Delta\phi^{\mu+1}=-\Delta\tau\,\mathbf{rhs}^\mu \qquad (19)$$

can therefore be solved in three consecutive steps:

$$\Delta\vec{\phi}^{\,*}=\mathbf{L}^{-1}\,(-\Delta\tau\,\mathbf{rhs}^\mu) \qquad (20)$$
$$\Delta\vec{\phi}^{\,**}=\mathbf{D}^{-1}\,\Delta\vec{\phi}^{\,*} \qquad (21)$$
$$\Delta\vec{\phi}=\mathbf{U}^{-1}\,\Delta\vec{\phi}^{\,**}\,. \qquad (22)$$

Furthermore it is possible to eliminate the calculation of the split flux jacobians and the subsequent multiplication with $\Delta\phi$ by applying a Taylor expansion to the fluxes [10].

The algorithm is completely vectorizable by reordering the grid points and storing them by diagonal planes $i+j+k=const.$ In that way, the vector length can also be increased with respect to a conventional i,j,k ordering.

For the finite–volume cell centred scheme, the evaluation of the fluxes at the cell faces, which appears on the right–hand side, **rhs**, is done by an approximate Riemann solver developed by Eberle [3]. The applied low dispersion scheme results in third–order spatial accuracy, being switched to first–order upwind at discontinuities.

Fluid Structure Coupling

Partitioned Procedures

In order to predict the dynamic response of a flexible structure in a fluid flow, the equations of motion of the structure and the fluid must be solved simultaneously. Since the governing equations of the fluid flow are highly nonlinear, the numerical solution via a fully coupled monolithic scheme is a quite difficult undertaking. Alternatively the fluid structure coupling can be accomplished by partitioned procedures [6]. This approach offers several appealing features including the ability to use well–established solution

methods within each discipline, simplification of software development efforts, and preservation of software modularity.

The physical interaction between the fluid and the structure can be understood in the following way [7]. During the time evolution of the flow field and the structure, the movement of the structure induces instantaneously a change in the flow. This influence is determined by the location and the speed of the flow boundary. Since the flow changes, the exerted force on the structure varies and the movement of the structure changes at the same time. Again, this last change implies a variation of the flow and the cycle starts again. It is obvious that the changes in the flow and the movements of the structure are coupled phenomena. They affect each other through the boundary conditions from structure to fluid and surface forces from fluid to structure. The underlying idea of a staggered solution strategy is to replace these continuous interactions with discrete ones over a time step from t^n to t^{n+1}. If we consider the flow field and the structure state to be known at timelevel t^n, a straightforward staggered algorithm is the following fluid structure coupling scheme 1 (FSC1).

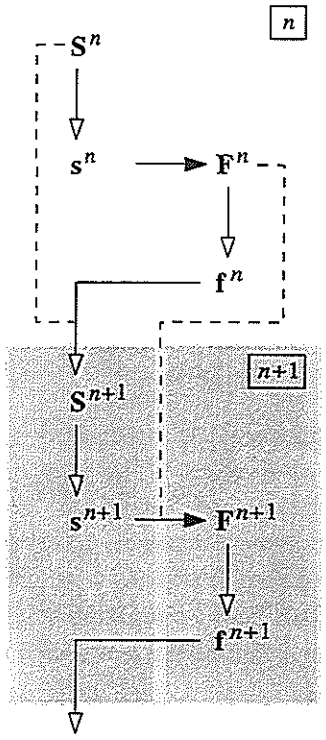

Figure 2: Fluid Structure Coupling Scheme 1

In the depicted scheme, the superscripts correspond to the timelevel. $\mathbf{S}$, $\mathbf{s}$, $\mathbf{F}$, and $\mathbf{f}$ represent the state of the structure, the boundary conditions for the fluid flow, the state of the fluid, and the forces on the structure surface, respectively. The filled arrows $\longrightarrow$ represent heavy computations with high computational costs, i.e. updating the state of the fluid with known boundary conditions. The hollow arrows $\longrightarrow\!\triangleright$ represent computations with moderate or low computational costs, i.e. advancing the structure state, computing the boundary conditions (here: the velocity–winder) for the flow, knowing the state of the structure or getting the surface force from the known variables of the fluid flow. The dashed lines indicate that additional information is needed. For example to determine the state of the structure $\mathbf{S}^{n+1}$ not only the forces $\mathbf{f}^n$ have to be known but also the previous state of the structure $\mathbf{S}^n$.

If we examine the FSC1 scheme more closely, an important fact will show up. The coupled system is advanced in time within the structure step $\mathbf{f}^n \longrightarrow\!\triangleright \mathbf{S}^{n+1}$. During this phase the flow variables are held constant, which means that compared to the structure the flow is a little late. Since the typical time of evolution for the fluid is considerably smaller than for the structure, we would prefer the structure rather than the fluid to be late. This can be accomplished by the FSC2 algorithm [7] shown in Figure 3. Here the coupled system is advanced from t^n to t^{n+1} during the fluid step $\mathbf{s}^n \longrightarrow \mathbf{F}^{n+1}$. The fluid manifests itself implicitly in the flow.

Additional attention has to be paid to the fact that we use an implicit solver for the fluid flow. To start the computation of $\mathbf{F}^{n+1}$, the flow variables at timelevel n, $\mathbf{F}^n$, but also the boundary conditions $\mathbf{s}^{n+1}$ must be known. To circumvent this problem, the following predictor–corrector algorithm was adopted. The structure state $\mathbf{S}^{n+1}$ is calculated with the values of $\mathbf{f}^n$ and $\mathbf{S}^n$ (predictor step) as it is done in the FSC1 scheme. Therefore $\mathbf{s}^{n+1}$ can be evaluated. Now we are able to perform the fluid step and advance the flow to timelevel $n+1$. With $\mathbf{f}^{n+1}$ known, the structure state $\mathbf{S}^{n+1}$ is calculated (corrector

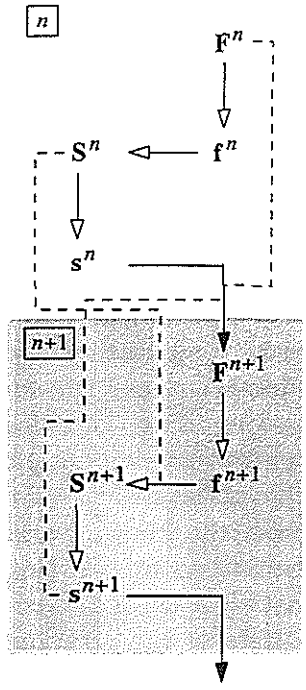

Figure 3: Fluid Structure Coupling Scheme 2

step). Another advantage of this approach, in terms of improved stability, is that the aerodynamic forces come implicitly into play when the structure evolves.

Implementation Issues

The coupling of the program modules itself, which means the exchange of data between the fluid and the structure solver can be established in two different ways.

First, if the source codes of both programs are at hand, they can be merged to a single program unit. This is obviously the fastest way of coupling, since the data has not really to be exchanged by the program parts. The disadvantage of this approach is that the modules cannot be exchanged nor can others be added with ease. When calculating a helicopter for example, an additional module for the prediction of helicopter noise could be considered.

If we want to retain the advantage of software modularity, given by the use of partitioned procedures, the programs must keep their independence. In this case they have to communicate with each other using routines provided by the operating system. The disadvantage of this method is that it's not as fast as the first one. This disadvantage will no longer be relevant if the computational time of a single module is considerably higher than the time needed for communication purposes. We have to assume that this is the case if we couple fluid with structure solvers by means of partitioned procedures. Another disadvantage is the higher administrative effort to synchronise the programs. In a monolithic program system this is in any case accomplished due to the sequential processing of the code. The supreme advantage in working with self–reliant programs is that they can be easily exchanged or added together with others.

In the present approach, the coupling is done by means of UNIX SVR4 interprocess communication (IPC) routines. In general there are three different ways of IPC: semaphores, message queues, and shared memory. Here we use message queues for synchronisation and data exchange — the data to be exchanged (synchronisation flags, forces, coordinates, velocity–winders) is transfered via strings. Thus we gain the advantage that the programs can still work with different internal representations of numbers, which would not be the case if shared memory IPC was used.

The fluid and structure parts of the code are written in Fortran 90, whereas the interface is written in C since it makes direct use of routines provided by the operating system.

Results and Discussion

Test–Case Definition

The validation of the coupled codes is done on a BO–105 model rotor. The test campaign at the DNW, carried out within the framework of the European cooperative research project HELINOISE, provides an extensive database for different flight conditions simulated with a 40% geometrically and dynamically scaled model of the BO–105 helicopter [9].

The rotor under consideration is a four–bladed hingeless rotor with a diameter of 4 m, a root

cut–out of 0.350 m, and a chord length of 0.121 m. The rotor blade uses a NACA 23012 airfoil with the trailing edge modified to form a 5 mm long tab to match the geometry of the full–scale rotor. The rotor blades have -8^o of linear twist, a standard square tip, and a solidity of 0.077. The nominal rotor operational speed is 1040 rpm.

The chosen test–case for the validation of numerical results is the low–speed level flight, HELINOISE DP–344. This test–case is characterized by an advance ratio of $\mu = 0.15$, a rotor thrust coefficient of $C_t = 0.00446$, and a hover tip Mach number of $Ma_h = 0.644$. Further details can be found in [9].

The elastic rotor blade is presently represented with the two degrees of freedom flapping and lagging for the dynamic part of the coupled procedure.

The flow field around the rotor blade is discretized with $65 \times 38 \times 26$ gridpoints. The computational grid in the physical space is shown in Figure 4. Using this grid, a performance of 600

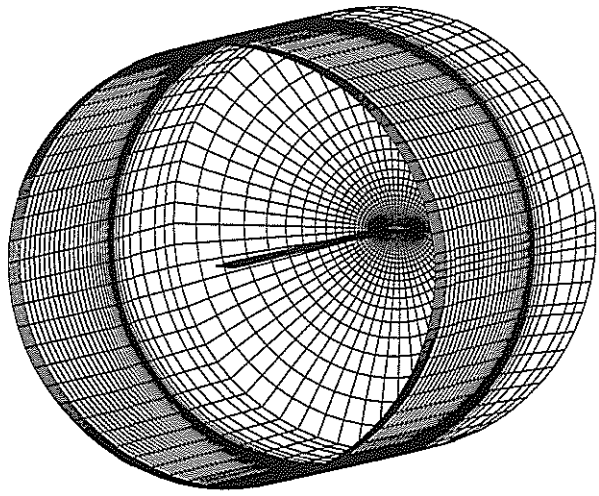

Figure 4: Computational Grid of the Blade

MFlops is achieved on a NEC–SX4 supercomputer, which results in approximately 12 minutes computational time per rotor revolution.

Calculation Procedure

The calculations were performed as follows. First, a converged solution for the rotor blade was determined with the dynamic solver STAN. At this stage of the procedure STAN uses the blade–element theory for the calculation of the aerodynamic forces. Part of this coupled 2D solution are the Fourier coefficients for β and ζ

$$\begin{aligned}\beta = \beta_0 &+ \beta_{1c} \cdot \cos\psi \;+ \beta_{1s} \cdot \sin\psi \\ &+ \beta_{2c} \cdot \cos 2\psi + \beta_{2s} \cdot \sin 2\psi \end{aligned} \tag{23}$$

$$\begin{aligned}\zeta = \zeta_0 &+ \zeta_{1c} \cdot \cos\psi \;+ \zeta_{1s} \cdot \sin\psi \\ &+ \zeta_{2c} \cdot \cos 2\psi + \zeta_{2s} \cdot \sin 2\psi \,, \end{aligned} \tag{24}$$

and also for the induced velocity

$$w_i = w_{i0} + w_{ic} \cdot \frac{r}{R} \cos\psi + w_{is} \cdot \frac{r}{R} \sin\psi \,. \tag{25}$$

These results can directly be fed into the aerodynamic solver INROT to obtain the solution of the uncoupled 3D flow field. This is the way we did the calculations in the past. Now the results of STAN serve as initial conditions for the fully coupled 3D aeroelastic computation. The aerodynamic solver is started with -60^o initial turn back of the blade in order to achieve a realistic flow field at $\psi = 0^o$ when the coupling process starts. The coupling is done over several rotor revolutions until a fully converged solution is achieved.

Results

The criterion for a converged solution is that the changes in the blade degrees of freedom from one rotor revolution to another do not exceed a certain limiting value, typically 10^{-6} in the order of magnitude.

$$\sum_{\psi=1^o}^{360^o} \left(\frac{\Delta\delta}{\delta}\right)^2 \leq \varepsilon \tag{26}$$

In Figure 5, the error sum defined by Equation (26) is shown for β and ζ. Both fluid structure coupling algorithms, FSC1 and FSC2, exhibit a stable convergence behaviour. This is

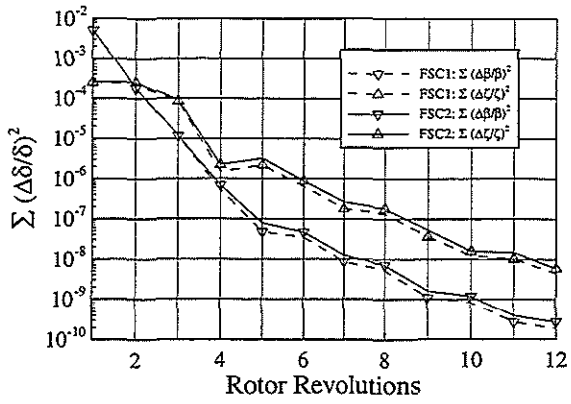

Figure 5: Transient Error Development

achieved through a special numerical damping of the starting conditions from one rotor revolution to the next. Indeed, if a subsequent revolution was started at $\psi = 0^o$ with the unmodified values of β and ζ at $\psi = 360^o$ there will be no convergence at all. The damping factor is adapted to $\Delta\delta$ in such a way that the damping is reduced to zero when the solution gets converged.

Figure 6 gives an exemplary comparison of the converged solutions for β, using the FSC1 and FSC2 schemes. It becomes clear that the converged solution is almost exactly the same for both schemes. This behaviour is also the same for ζ and any other solution variables. It is not yet tested if this situation will remain unchanged when additional degrees of freedom or different flight conditions are taken into consideration. However, relating to the discussion in the section about 'Partitioned Procedures' the author strongly recommends the use of FSC2.

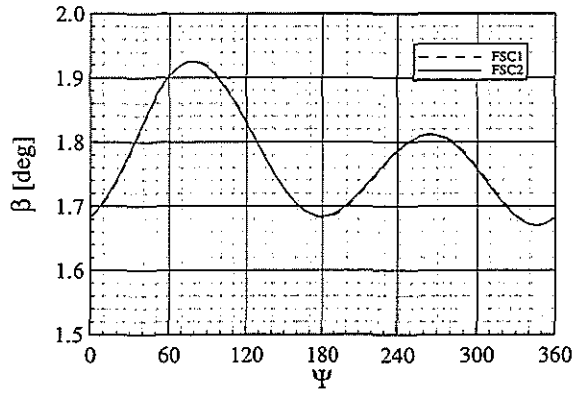

Figure 6: Comparison of Staggered Procedures

Finally, Figures 7 and 8 present the convergence history of β and ζ. Good convergence behaviour is in any case achieved after four consecutive revolutions.

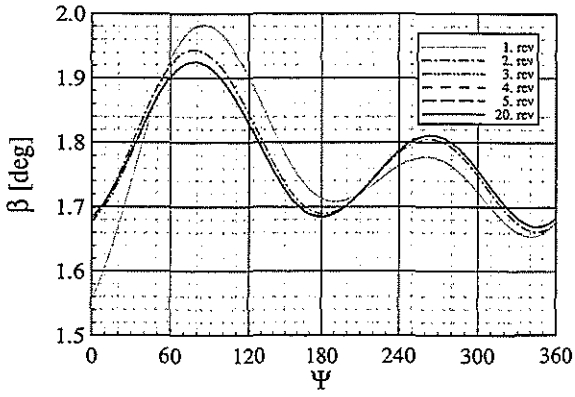

Figure 7: Convergence Study of Flapping

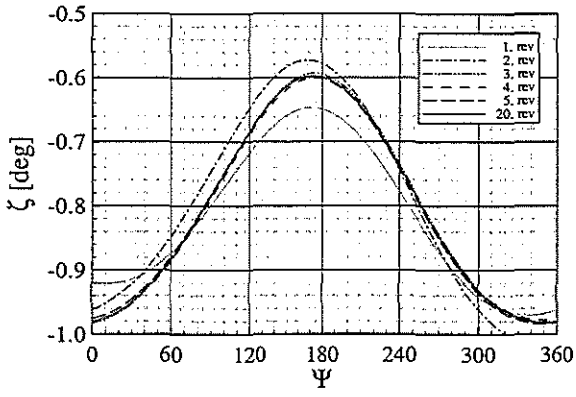

Figure 8: Convergence Study of Lagging

Now we will focus on the question, how the dynamic behaviour of the rotor blade will change if we solve the complete three–dimensional, inviscid flow field instead of using 2D blade–element theory in order to calculate the aerodynamic forces acting on the blade. Figure 9 illustrates the variation of β over ψ for both cases. It is obvious that the amplitude changes drastically if the 3D Euler solver is used. This tendency can also be seen if we take a look at the corresponding Fourier coefficients.

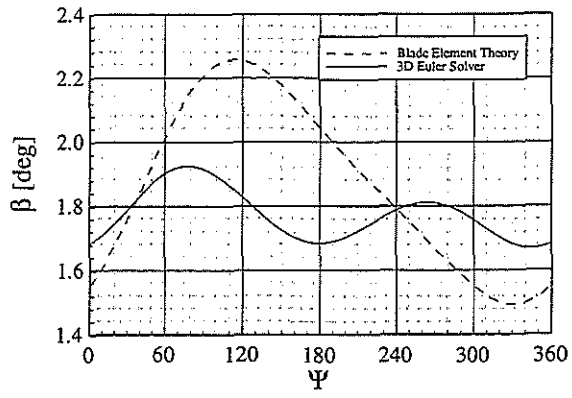

Figure 9: 2D vs. 3D Aerodynamic Modelling

	β_0	β_{1c}	β_{1s}	β_{2c}	β_{2s}
2D	1.867	− 0.243	0.266	− 0.069	− 0.000
3D	1.774	0.007	0.053	− 0.089	− 0.030

The 0^{th} harmonic coefficient decreases about only 5%, whereas the 1^{st} harmonic coefficients decrease about 97% in β_{1c} and 80% in β_{1s}. In light of the fact that the experimental rotor operated with zero flapping (due to cyclic pitch control), this experimental handicap is now reproduced a lot better.

Figure 10 shows the above mentioned comparison for the second degree of freedom, ζ. The

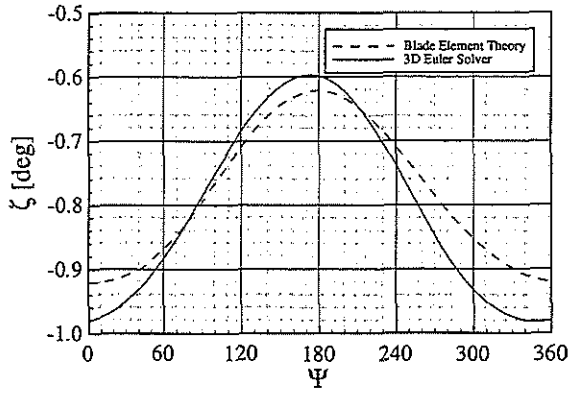

Figure 10: 2D vs. 3D Aerodynamic Modelling

lagging angle is less affected by the dimensionality of the aerodynamic modelling, which is quite obvious if we take a look at the following table.

	ζ_0	ζ_{1c}	ζ_{1s}	ζ_{2c}	ζ_{2s}
2D	− 0.780	− 0.150	− 0.005	0.010	− 0.004
3D	− 0.803	− 0.192	0.030	0.013	− 0.002

Comparisons between the experimental chordwise pressure distributions and calculated results are presented in Figure 11 for various azimuthal and radial positions. Very good agreement between predicted and measured distributions is observed in most cases. In cases with more or less significant deviations from flight data ($\psi = 90^o$ at 97%, $\psi = 180^o$ at 97%, $\psi = 270^o$ at 75%) the coupled results tend to be closer to the experimental data.

A better agreement will probably be achieved if a more sophisticated modelling of the wake and a finer grid is introduced. Both concerns will be dealt with in future work.

The resulting inviscid forces and moments at the blade are obtained when the pressure is integrated over the blade surface, see Equations (2) and (3). They are shown in Figure 12 over a rotor revolution.

The origin of the underlying coordinate system is the quarter chord point at the blade root. The x–axis points towards the trailing edge, the y–axis to the blade tip, and the z–axis upwards.

Except for f_y, the results obtained with the coupled 3D Euler analysis cannot be achieved by other methods, nor by the uncoupled 3D Euler solution neither by the coupled 2D blade–element approach. Due to the two–dimensionality of the blade–element approach, f_y cannot be investigated and is therefore zero. The large differences in m_y stem from the fact that the computational grid for the Euler calculations was designed without tab. To capture the effects of the tab accurately, it has to be resolved with a very fine grid spacing in its immediate vicinity. Furthermore, viscous effects in the flow should then be accounted for by the use of a Navier–Stokes solver.

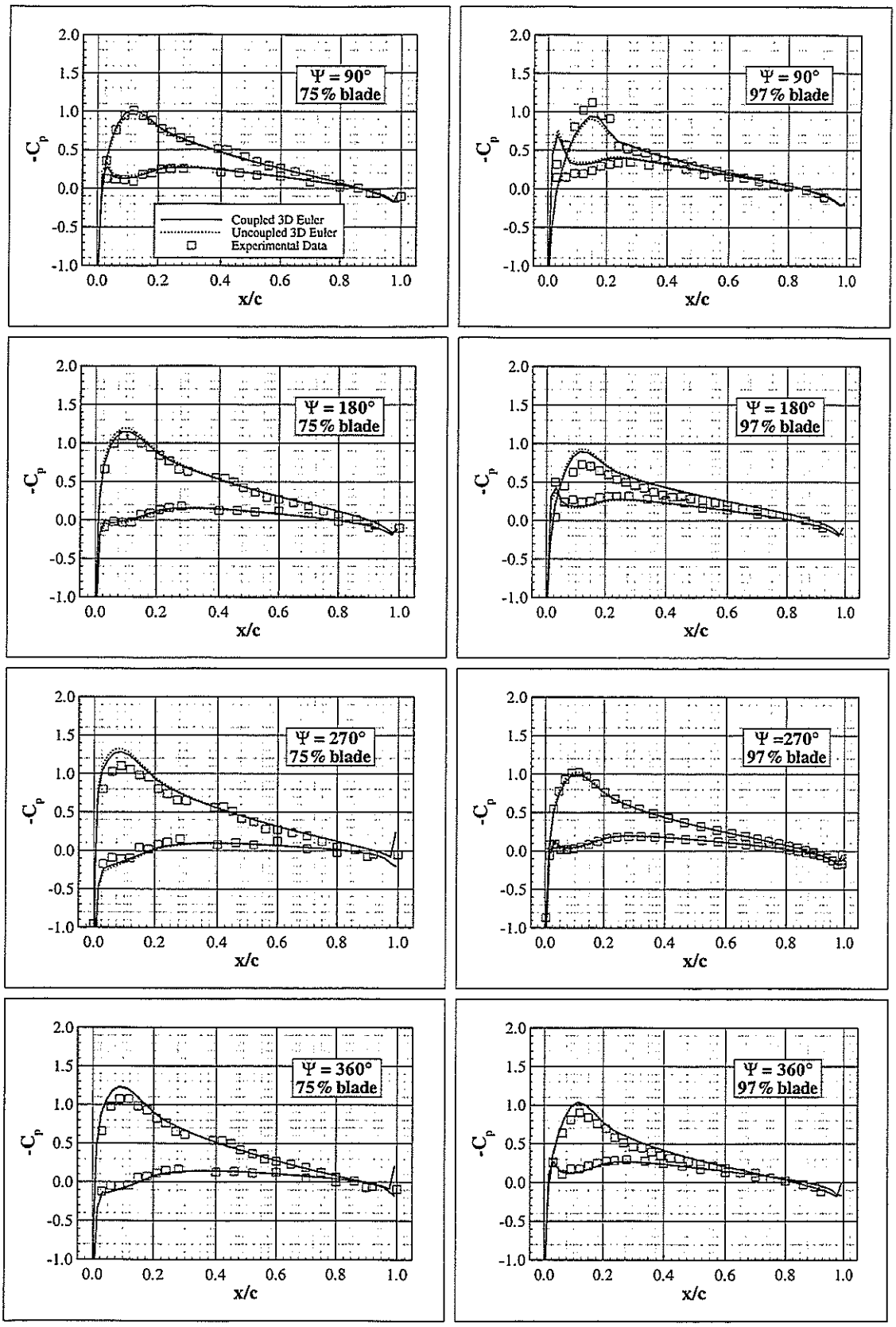

Figure 11: Chordwise Pressure Distribution

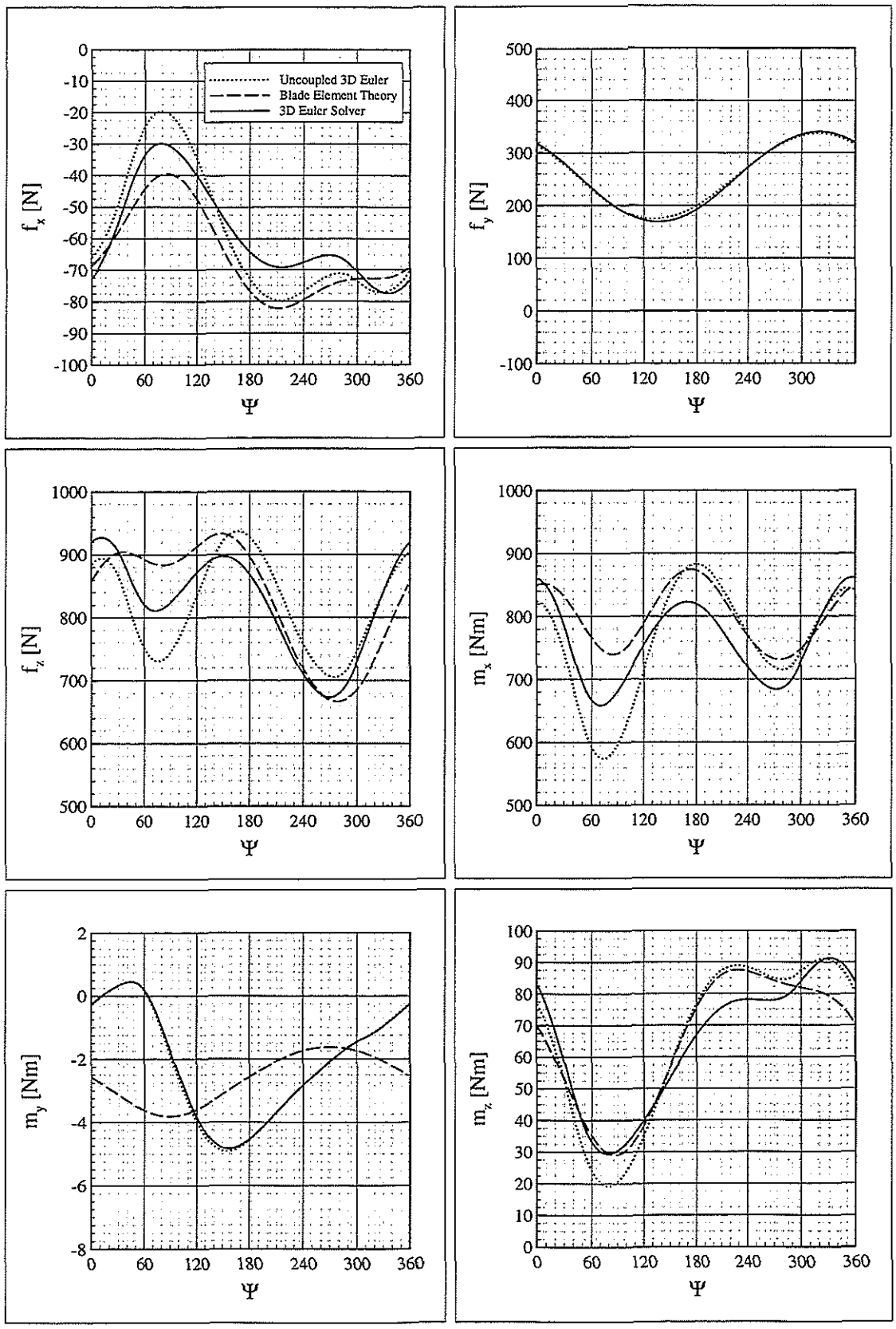

Figure 12: Resulting Forces and Moments in the Quarter Chord Coordinate System

Conclusions

In this paper an approach for the coupling of dynamic and aerodynamic methods for the calculation of helicopter rotor characteristics is presented. The dynamic properties of the rotor blades are represented by their first natural modes and frequencies, whereas the flow field is described by the three–dimensional Euler equations.

Two fundamentally different fluid structure coupling schemes are discussed and investigated. The implementations of the schemes exhibit a monotone and stable convergence behaviour during the solution process.

The validation of the aeroelastic system is done on a BO–105 model rotor in low–speed level flight. The agreement between the experimental data and the calculated results is rather good, even from a quantitative point of view. Especially the fully coupled results are in a significantly better agreement with the experiment than the uncoupled calculations.

Future work will be done on the application of the developed methods to other test–cases, especially high–speed level flight situations where shocks occur at the advancing blade. Furthermore, a more sophisticated modelling of the wake has to be considered. Therein we will investigate the use of a free–wake model in comparison to implicitly capturing the wake by means of a chimera technique.

Acknowledgement

This work was supported by the BMBF under the reference number 20H–9501–B. The author would like to thank Eurocopter Deutschland (ECD) for their support and for providing him with the structural model for the dynamic calculations.

References

[1] Buchtala, B.: *STAN Programmbeschreibung. Theoretische Grundlagen zur Berechnung des Hauptrotors.* Internal Report, Institut für Aero– und Gasdynamik, Universität Stuttgart, Germany, August 1996.

[2] Chen, C.L., McCroskey, W.J., and Obayashi, S.: *Numerical Solutions of Forward–Flight–Rotor Flow using an Upwind Method.* Journal of Aircraft, vol. 28, no. 6, pp 374–380, June 1991.

[3] Eberle, A.: *MBB–EUFLEX. A New Flux Extrapolation Scheme Solving the Euler Equations for Arbitrary 3–D Geometry and Speed.* Report MBB–LKE122–S–PUB–140, MBB, Ottobrunn, Germany, 1984.

[4] Huber, H.: *Some Objectives in Applying Hingeless Rotors to Helicopters and V/STOL–Aircraft.* AGARD–CP–111, AGARD Conference on Aerodynamics of Rotary Wings, Marseilles, France, September 1972.

[5] Jameson, A. and Yoon, S.: *LU Implicit Schemes with Multiple Grids for the Euler Equations.* AIAA Paper 86–0105, 24th AIAA Aerospace Sciences Meeting, Reno, Nevada, January 1986.

[6] Park, K.C. and Felippa, C.A.: *Computational Methods for Transient Analysis.* In T. Belytschko and T.J.R. Hughes, editors, *Partitioned analysis of coupled systems*, pp 157–219, North–Holland Pub. Co., 1983.

[7] Piperno, S.: *Simulation numérique de phénomènes d'interaction fluide–structure.* Ph.D. Thesis, Ecole Nationale des Ponts et Chaussées, France, June 1995.

[8] Reichert, G. and Oelker, P.: *Handling Qualities with the Bölkow Rigid Rotor System.* 24th Annual National Forum of the American Helicopter Society, May 1968.

[9] Splettstoesser, W.R., Junker, B., Schultz, K.–J., Wagner, W., Weitemeyer, W., Protopsaltis, A., and Fertis, D.: *The HELINOISE Aeroacoustic Rotor Test in the DNW – Test Documentation and Representative Results.* DLR–Mitteilung 93–09, Braunschweig, December 1993.

[10] Wehr, D., Zerle, L., and Wagner, S.: *Coupling Euler and Potential Methods for the Calculation of Rotors in Unsteady Forward Flight.* 22nd European Rotorcraft Forum, pp 59.1–59.12, Brighton, September 1996.